Polymer 137 (2018) 370–377

Contents lists available at ScienceDirect

Polymer

journal homepage: www.elsevier.com/locate/polymer

ZnO/carbon hybrids derived from polymer nanocomposite precursor materials for pseudocapacitor electrodes with high cycling stability

Yepin Zhao [b, 1], Zongyu Wang [a, 1], Rui Yuan [a], Yu Lin [b], Jiajun Yan [a], Jianan Zhang [a, b, c], Zhao Lu [b], Danli Luo [b], Joanna Pietrasik [d], Michael R. Bockstaller [a, *], Krzysztof Matyjaszewski [b, **]

[a] Department of Materials Science and Engineering, Carnegie Mellon University, Pittsburgh, PA 15213, United States
[b] Department of Chemistry, Carnegie Mellon University, Pittsburgh, PA 15213, United States
[c] School of Chemistry and Chemical Engineering, Anhui University, Hefei 230601, People's Republic of China
[d] Institute of Polymer and Dye Technology, Technical University of Lodz, Stefanowskiego 12/16, 90 924 Lodz, Poland

ARTICLE INFO

Article history:
Received 15 October 2017
Received in revised form
1 January 2018
Accepted 6 January 2018
Available online 9 January 2018

Keywords:
Nanocomposite
Nanocarbon
Capacitor

ABSTRACT

A facile new route for fabricating carbon/zinc oxide (carbon/ZnO) hybrid materials suitable for pseudocapacitor electrodes with high cycling stability is presented. The synthesis of carbon/ZnO nanocomposites involved the uniform dispersion of octylamine (OA) capped ZnO nanocrystals into poly(styrene-*r*-acrylonitrile) (PSAN) copolymers and the subsequent pyrolysis of the nanocomposite precursor material to form the carbon/ZnO hybrid. PSAN copolymers with two different chain lengths were prepared to illustrate the effect of chain length on structure and properties of the composites. For all cases, the pyrolysis of ZnO-OA/PSAN precursor blends resulted in the formation of disperse ZnO/carbon core-shell hybrid structures. The accessible surface area was found to increase with molecular weight of matrix chains. The ZnO/carbon composites exhibited a specific capacitance of 145 F g^{-1} at the scan rate of 2 mV s^{-1}. In addition, 91% of the initial capacitance was obtained after 10,000 charge/discharge cycles. The versatility of the synthetic process should render the presented method attractive for the fabrication of a wide range of carbon/transition metal oxide hybrid materials.

1. Introduction

The development of benign energy resources as well as storage systems presents one of the most pressing societal needs [1–4]. Electrochemical capacitors (ECs) are among the key technological systems that define the state of the art in electrical energy storage systems [1–6]. Electric double-layer capacitors (EDLCs), also known as supercapacitors, have garnered particular interest. This is because they offer high power density (1–2 orders of magnitude higher than that of batteries), fast charging and discharging, short response time, superior cycle lifetime (2–3 orders of magnitude better than that of batteries), and high reliability [1–7]. A sign of the reliability and utility of supercapacitors is their use in a variety of applications, including portable consumer electronics, computer memory backup systems, power for the next generation all electric vehicles, industrial-scale power and energy management [8]. However, a major bottleneck that limits the acceptance of existing supercapacitors in many high value applications, including energy storage devices, is their low energy storage density, generally an order of magnitude lower than that of batteries. Therefore, improving the energy density, while maintaining the high power density and cycling stability for supercapacitor devices, remains the primary challenge in the field [3,9].

As another type of ECs, pseudocapacitors utilize fast and reversible redox reactions at the surface of the electroactive material for charge storage [10–12]. In fact, in addition to capacitive improvements, pseudocapacitive materials are able to provide much higher energy density than carbon based materials in electric double layer capacitors, resulting in increased interest in these systems [10–12]. Several active pseudocapacitive materials, including transition metal oxides and conducting redox polymers, have been developed [13–20]. Their high energy density along with

* Corresponding author.
** Corresponding author.
E-mail addresses: bockstaller@cmu.edu (M.R. Bockstaller), km3b@andrew.cmu.edu (K. Matyjaszewski).
[1] Y.Z. and Z.W. contributed equally to the work.

https://doi.org/10.1016/j.polymer.2018.01.024
0032-3861/

fast and reversible redox reactions at the electrode surface can significantly enhance the specific capacitance [18,19,21]. The ability of pseudocapacitors based on hybrid composite materials with a porous carbon structure to maintain high power density and fast charge–discharge rate has drawn significant research attention. Recently, hybrid composites based on transition metal oxides, including iron oxide (Fe_2O_3) [22,23], cobalt oxide (CoO, Co_3O_4) [24,25] and manganese oxide (MnO_2) [26,27], have been evaluated as pseudocapacitor electrodes [28]. Unfortunately, most of these specific metal oxides suffer poor cycling stability and reversibility during the charge–discharge process.

Zinc oxide has drawn interest as transition metal oxide for the fabrication of pseudocapacitors due to its low-cost, environmental friendliness, and ease of synthesis [29–31]. Integration of ZnO with other pseudocapacitive materials resulted in remarkable capacitance performance. However, existing materials were shown to suffer from poor cycling stability. One strategy to address this shortcoming is the integration of ZnO with materials that exhibit high cycling stability. In particular, ZnO/carbon hybrid materials have been pursued since carbon materials usually display excellent rate performances, reversibility, and stability [23,32–42]. However, although experiments on ZnO/carbon hybrids did show promising results, the cycling stability of tested materials was found to be a challenge. This was interpreted to be a consequence of the non-uniform and phase separated structure of the hybrid material. High capacitance values (>300 F g^{-1}) and generally superior performances were reported for ZnO/carbon nanotubes and ZnO/graphene nanofiber hybrids [43,44]. However, the costs of materials and complexity of the synthesis limit the application of these type of materials [28]. Thus the development of effective strategies for the preparation of ZnO/carbon composites with high degree of morphological control for use as electrochemical capacitors remains an important goal.

In this contribution, we report a facile method to fabricate ZnO/carbon composites based on the pyrolysis of uniformly structured ZnO/polymer nanocomposites. Octylamine (OA) capped ZnO nanocrystals were prepared by thermal decomposition of zinc 2-ethylhexanoate in the presence of octylamine [45–48]. Poly(-styrene-*r*-acrylonitrile) copolymers (PSAN) were synthesized through ARGET ATRP (Activator ReGenerated by Electron Transfer Atom Transfer Radical Polymerization) [49–56]. The AN units in the copolymers can efficiently crosslink and form porous carbon structures [57,58]. ZnO/PSAN hybrid materials with uniform microstructure were prepared by solution casting from THF. The uniform microstructure was retained during subsequent pyrolysis of the nanocomposite template to form the final carbon/ZnO hybrids. The electrochemical performance of carbon/ZnO hybrid electrodes was determined by evaluation of the specific capacitance and cycling stability. Gravimetric capacitance of 145 F g^{-1} was achieved and 91% of the initial capacitance was maintained after 10,000 charge–discharge cycles. The viability of material synthesis and processing, along with the performance and lifetime of the materials in pseudocapacitor applications suggest the potential of these novel materials as candidates for electrochemical applications.

2. Experimental

Materials and Methods Monomers: styrene (S, 99%, Aldrich) and acrylonitrile (AN, 99%, Aldrich) were purified by passing through a column filled with basic alumina to remove the inhibitor. Tris(2-dimethylaminoethyl)amine (Me_6TREN, 99%, Alfa), zinc 2-ethylhexanoate ($Zn(EH)_2$, 80% in mineral spirits, Alfa), anisole (99%, Aldrich), methylene chloride (DCM, 99.5%, Fisher), carbon black, acetylene (100% compressed, 99.9%, Alfa), *N*-methylpyrrolidone (NMP, 99.5%, Sigma-Aldrich), poly(vinylidene fluoride) (M_w~180,000, M_n~71,000, Aldrich), zinc oxide (ZnO, 18 nm, 99.95%), tetrahydrofuran (THF, 99%, VWR), methanol (99%, VWR), hexane (99%, VWR), acetone (99%, VWR), *N*,*N*-dimethylformamide (DMF, 99%, VWR), ethyl 2-bromoisobutyrate (EBiB, 98%, Aldrich), copper(II) bromide ($CuBr_2$, 99%, Aldrich), diphenyl ether (DPE, 99%, Aldrich), tin(II) 2-ethylhexanoate ($Sn(EH)_2$, 95%, Aldrich), and octylamine (OA, 99%, Aldrich) were used as received without further purification.

Synthesis of OA-capped ZnO nanoparticles OA-capped ZnO NPs were synthesized as reported by Epifani and Weber [45,46], by the procedure illustrated in Scheme 1. The resulting product was dispersed in THF and a stock solution was prepared for use in further experiments. ZnO NPs are stabilized by surfactant octylamine (OA) ligands. The binding of OA ligands likely involves a coordination bond between the amino group and positively charged Zn^{2+} on the particle surface.

Synthesis of PSAN copolymers The copolymerization of S and AN by ATRP had been well studied in previous work [56,59]. Low molecular weight (MW) PSAN ($M_n = 1800$ with $M_w/M_n = 1.18$) and high MW PSAN ($M_n = 8000$ with $M_w/M_n = 1.21$) were synthesized via ARGET ATRP using EBiB as an initiator, $CuBr_2$/Me_6TREN as precursor of the catalytic complex and $Sn(EH)_2$ as reducing agent using the following general procedure. Styrene (S) (16 mL, 139.85 mmol), acrylonitrile (AN) (5.5 mL, 83.91 mmol), Me_6TREN (0.075 mL, 0.28 mmol), anisole (7.2 mL), EBiB(1.37 mL, 9.32 mmol), and 0.03 mol L-1 solution of $CuBr_2$ in DMF (0.5 mL, 0.015 mmol) were added to a dry 50 mL Schlenk flask. After the flask was sealed, the resulting solution was bubbled with N_2 for 30 min. Then, 300 mM of $Sn(EH)_2$ solution in anisole (1 mL, 0.30 mmol) was slowly added to the flask to reduce a fraction of the $CuBr_2$ and activate the polymerization. The flask was subsequently placed in an oil bath set at 60 °C, and the reaction mixture was kept at that temperature for the desired time. Then the reaction mixture was exposed to air to stop the polymerization and the product was precipitated by addition of the solution to cold hexane, filtered and dried in air.

The synthesis of the copolymers with different molecular weights was similar to the procedure described above, but with different targeted degrees of polymerization, as reported previously [56,59,60].

Synthesis of ZnO/carbon nanocomposites A typical procedure for synthesizing ZnO/carbon composite precursors consisted of dissolving PSAN copolymers and of OA-Capped ZnO NPs in 100 mL THF in a 200 mL beaker. To achieve uniform and homogenous solid powder mixtures, the beaker was covered with Al foil with pin holes on the top allowing the THF solvent to slowly evaporate under ambient condition over 2 days. The mixture was then transferred to a vacuum oven set at 100 °C for 2 days to remove all residual solvent. Yellow powders were obtained for use in further

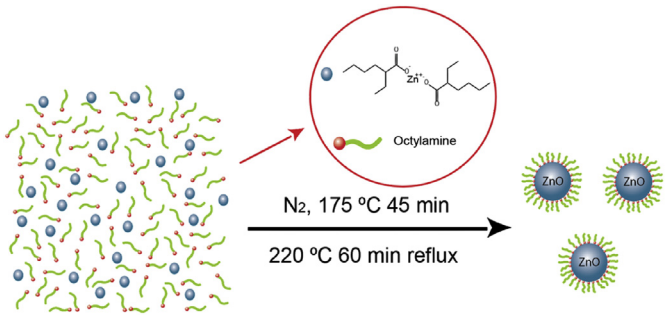

Scheme 1. Synthesis of OA-capped ZnO NPs using two step pyrolysis reaction of zinc 2-ethylhexanoate in the presence of OA.

experiments. The intimate mixture of PSAN/OA-capped ZnO powders were pyrolyzed in a tube furnace at 800 °C for 3 h under N_2 flow with 10 °C min^{-1} heating rate. Nanocomposite mixtures with distinct molecular weight of the polymer matrix were compared. PSAN with $M_n = 8000$ was identified as the ideal polymer molecular weight to enable both dispersion of ZnO and material integrity during pyrolysis. The final products were prepared by pyrolysis of mixtures with different compositions of ZnO and PSAN, which were named by ZnO-$C_{2k\text{-}4}$ (synthesized by 4 g of M_n~2000 PSAN), ZnO-$C_{8k\text{-}2}$ (synthesized by 2 g of M_n~8000 PSAN), ZnO-$C_{8k\text{-}2.5}$ (synthesized by 2.5 g of M_n~8000 PSAN), respectively, are listed in Table 1. A pure carbon sample was prepared by pyrolysis of M_n~8000 PSAN under same conditions for comparison.

Characterization Transmission electron microscopy (TEM) was carried out using a JEOL 2000 EX electron microscope operated at 200 kV. Scanning electron microscope (SEM) was carried out using a quanta 600 environmental scanning electron microscope. The average sizes of the ZnO NPs were determined from statistical analysis of TEM micrographs using ImageJ software. Dynamic light scattering (DLS) using a Malvern Zetasizer Nano ZS was performed to confirm the results obtained from TEM analysis. It was also employed to determine volume-weighted average hydrodynamic diameters and distribution. A Philips X'Pert (Philips Analytical, Netherlands) X-ray diffractometer (XRD) (Cu-Kα radiation) was operated at 45 kV and 40 mA in grazing incidence mode to characterize the structure and crystallinity of the formed composite materials. Thermogravimetric analysis (TGA) with TA Instruments 2950 was used to measure the fraction of ZnO in the hybrids. The data were analyzed with TA Universal Analysis. The TGA plots were normalized to the total weight after holding the samples at 120 °C. The copolymers were characterized by size exclusion chromatography (SEC) and nuclear magnetic resonance (NMR) spectroscopy, the glass transition temperature (T_g) of PSAN polymers with different molecular weight were measured by differential scanning calorimetry (DSC) with TA Instrument QA-2000, the same procedure was run three times, each involving the following steps: (1) hold at 25 °C for 2 min, (2) heat to 160 °C at a rate of 10 °C/min, (3) hold for 2 min, and (4) cool to 25 °C, the DSC data were analyzed with a TA Universal Analysis instrument, and T_g was directly acquired, the detailed information is included in the Supporting Information. Surface areas of ZnO/carbon nanocomposite were measured by a Brunauer-Emmett-Teller (BET) Gemini VII 2390 Surface Area Analyzer.

Electrochemical Measurements A symmetric two-electrode system was applied in the electrochemical tests. The electrodes were prepared by mixing 85 wt% of the ZnO/carbon samples, 5 wt% acetylene black as conductive additive, and 10 wt% of poly(-vinylidene fluoride) as binder. The mixture was homogenized in *N*-methylpyrrolidone (NMP) by sonication for 10 min and the slurry was deposited on carbon paper with a diameter of 13 mm and dried at 100 °C in a vacuum oven over 24 h. For comparison, ZnO-$C_{8k\text{-}2}$, ZnO-$C_{8k\text{-}2.5}$ and ZnO-$C_{8k\text{-}2}$ were made into electrodes. And to determine the contribution of ZnO and C and synergistic effect of the composite, ZnO nanoparticles and carbon made from PSAN polymers were made into electrodes separately. Electrochemical cells were prepared using a Teflon Swagelok. 1 M KOH was used as electrolyte and a porous polyolefin separator (Celgard Inc.) was soaked with KOH electrolyte and placed between the electrodes.

The electrochemical measurements were carried out on a potentiostat (Biologic SP-300). The cyclic voltammetry (CV) curves were obtained at various scan rates from 2 mV s^{-1} to 2000 mV s^{-1} in the range of 0–1 V. Galvanostatic charge-discharge (GCD) curves were obtained at various current densities from 0.1 A g^{-1} to 20 A g^{-1}. Electrochemical impedance spectroscopy (EIS) measurements were performed in the frequency range of 0.1 Hz–800 kHz with sinusoidal signal of 10 mV. For each sample, 10 measurements were repeated to confirm its reproducibility [61].

For samples containing ZnO, the possible mechanisms of pseudocapacitance derives from redox reactions which are governed by the intercalation and deintercalation of K^+ from electrolyte into ZnO [42]: $ZnO + K^+ + e^- \leftrightarrow ZnOK$

The gravimetric capacitance of each electrode, C_{sp}, is then determined from the cyclic voltammetry (CV) via the following equation:

$$C_{sp} = \frac{\int IdV}{\nu m V} \quad (1)$$

The gravimetric capacitance of each electrode, C_{sp}, from the galvanostatic charge-discharge (GCD) curves is determined via equation (2):

$$C_{sp} = \frac{2I\Delta t}{mV} \quad (2)$$

In the equations, $\int IdV$ is the area of CV curves; ν (V s^{-1}) is the voltage scan rate; Δt (s) is the discharge time; I/m is the scan rate (A g^{-1}) where m (g) is the mass of each electrode and I (A) is the current applied}; V (V) is the voltage window.

3. Results and discussion

ZnO/carbon hybrids were prepared by pyrolysis of a mixture of OA-capped ZnO nanoparticles and PSAN copolymer. The OA-capped ZnO nanoparticles were synthesized by the thermal decomposition of zinc 2-ethylhexanoate in a mixture of OA and diphenyl ether at 220 °C. The ZnO nanoparticles obtained by this method have narrow particle size distribution and good solubility in tetrahydrofuran (THF) or hexane as seen in Figure S2. Polyacrylonitrile (PAN) is well established as a precursor for carbon composite materials than can be obtained from the polymer via pyrolysis [62,63]. However, PAN polymers are not soluble in non-polar solvents, such as THF or hexane, which are good solvents for OA-capped ZnO nanoparticles. To achieve miscibility with the ZnO-OA nanoparticle system, a random copolymerization of AN with the unpolar monomer styrene (S) was performed. PSAN copolymers with a molar composition of S:AN = 3:1 were synthesized by ARGET-ATRP and found to be soluble in THF. Solvent cast methods could now be applied to obtain well-dispersed ZnO/polymer mixtures suitable as a precursor of the desired hybrid carbon materials. Two different copolymers with narrow molecular weight distributions were prepared, one with $M_n = 1800$ and another with $M_n = 8000$ to evaluate the role of matrix molecular weight on structure formation during pyrolysis (see Fig. S1). Three dilute THF solutions, with different polymers and compositions were prepared and the ratios are listed in Table 1. After removing all solvent by atmospheric evaporation followed by vacuum annealing, yellow powders for low molecular weight (MW) PSAN-based mixtures and films for higher MW PSAN were obtained, which were further characterized by TGA. The three ZnO/carbon

Table 1
Preparation of nanocomposites from OA-capped ZnO and PSAN precursors.

Entry	OA capped ZnO (g)	PSAN (g)	M_n,[a]	M_w/M_n[a]
ZnO-$C_{2k\text{-}4}$	3	4	1800	1.18
ZnO-$C_{8k\text{-}2}$	3	2	8000	1.21
ZnO-$C_{8k\text{-}2.5}$	3	2.5	8000	1.21

[a] Number-average molecular weights (M_n) and molecular weight distributions (M_w/M_n) of the polymer ligands were measured by SEC.

composite samples had similar carbon contents, between 7.6 and 8.4 wt%, Fig. S3.

We note that the choice of appropriate temperatures for successful pyrolysis of materials is relevant in the process described above. For example, Lee and coworkers reported the formation of elemental zinc (via carbothermic reduction of ZnO) are temperatures in excess of 1000 °C [64,65]. Thus, to avoid the formation of elemental zinc pyrolysis was performed at 800 °C. XRD patterns of ZnO/carbon nanocomposite samples from the different precursors are shown in Fig. 1; the results suggest the exclusive presence of ZnO. Similar XRD patterns were obtained from ZnO-$C_{2k\text{-}4}$, ZnO-$C_{8k\text{-}2}$, and ZnO-$C_{8k\text{-}2.5}$. The patterns can be interpreted as Wurtzite structure for the ZnO (JCPDS No. 36–1451) with no diffraction peak attributable to the carbon species. The well-fitted ZnO peaks in the patterns demonstrate that carbon formation does not influence the crystal structure of the ZnO. However, ZnO-$C_{2k\text{-}4}$ exhibited much broader peaks than those observed from ZnO-$C_{8k\text{-}2}$ and ZnO-$C_{8k\text{-}2.5}$. We can estimate the crystallite size D of ZnO-$C_{2k\text{-}4}$, ZnO-$C_{8k\text{-}2}$ and ZnO-$C_{8k\text{-}2.5}$ particles from the (110) plane diffraction peak ($2\theta = 56.6°$), by using the Scherrer equation $D = 0.9(\lambda/\beta)\cos\theta$ (where $\lambda = 0.154$ nm is the wavelength of X-rays and β is the true half peak width of the X-ray diffraction lines). Following to this process the sizes of the ZnO nanoparticles follow to be 5 nm, 25 nm, and 23 nm for ZnO-$C_{2k\text{-}4}$, ZnO-$C_{8k\text{-}2}$, and ZnO-$C_{8k\text{-}2.5}$, respectively [42]. Since all OA-capped ZnO nanoparticles precursors had the same size, the different sizes have to be attributed to changes of crystal size during the calcination process. Specifically, we hypothesize that the different dimensions of particles in the pyrolyzed products reflect different levels of aggregation of OA-capped ZnO particles in the polymer matrix. The results thus suggest that a low molecular weight matrix supports the stable dispersion of OA-capped ZnO particles and thus reduces aggregation and crystal coarsening during the pyrolysis process (although it should be noted that the lower particle concentration in the ZnO-$C_{2k\text{-}4}$ system could also contribute to the reduced aggregation).

Scanning and transmission electron microscopy (SEM and TEM) were used to further elucidate the microstructure of ZnO-$C_{2k\text{-}4}$, ZnO-$C_{8k\text{-}2}$, and ZnO-$C_{8k\text{-}2.5}$ composite materials. SEM images (Fig. 2a, c, and 2e) reveal a distinctive difference on the surface morphology of the three material systems. Specifically, the SEM

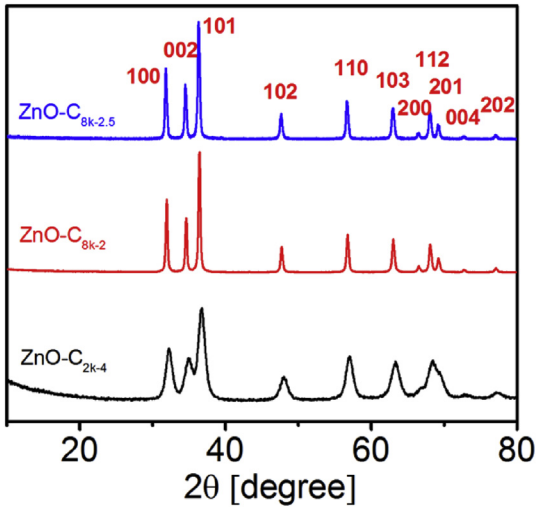

Fig. 1. XRD patterns of ZnO/carbon nanocomposites. The patterns reveal characteristic ZnO Wurtzite structure (JCPDS No. 36–1451). The increasing peak width indicates a decrease of crystallite dimension for samples prepared from lower molecular weight PSAN precursor (ZnO-$C_{2k\text{-}4}$).

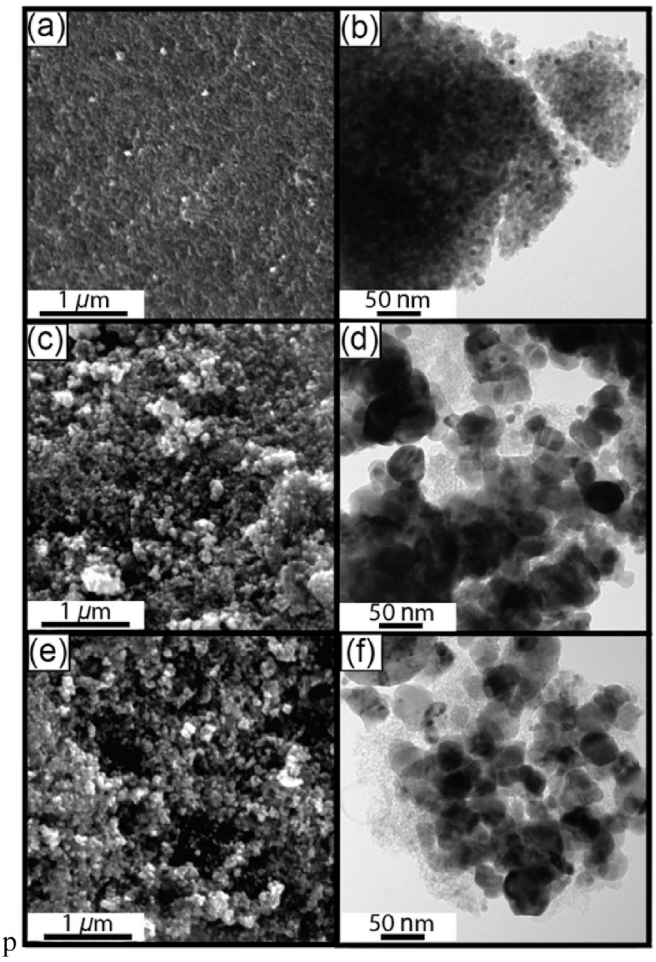

Fig. 2. Microstructural characterization of ZnO/carbon nanocomposites. SEM images (a), (c), and (e) showing non-porous surface of ZnO-$C_{2k\text{-}4}$ (a); porous structure of ZnO-$C_{8k\text{-}2}$ (c) and porous structure of ZnO-$C_{8k\text{-}2.5}$ (e). TEM images (b), (d), and (f) showing small size of particles with non-porous carbon shell in ZnO-$C_{2k\text{-}4}$ (b); large size of particles with porous carbon shell in ZnO-$C_{8k\text{-}2}$, but still some non-porous components exist (d); large size of particles with porous carbon shell in ZnO-$C_{8k\text{-}2.5}$ (f).

image of ZnO-$C_{2k\text{-}4}$ (see Fig. 2a) reveals a more contiguous film with a smooth non-porous surface. Such a structure is not expected to benefit applications as supercapacitor electrodes due to the reduced accessible surface area. In contrast, ZnO-$C_{8k\text{-}2}$ and ZnO-$C_{8k\text{-}2.5}$ (see Fig. 2c and e) exhibited a coarse particulate morphology, which indicates the formation of a more porous carbon matrix during the pyrolysis. TEM images (Fig. 2b, d, and 2f) further confirmed the differences in carbon morphology between low and high MW matrix materials. TEM images for low MW ZnO-$C_{2k\text{-}4}$ (see Fig. 2b) reveal a particle size of 4–7 nm for ZnO particles (*i.e.* approximately equal to the pristine OA-capped ZnO). Particles appear uniformly distributed within a dense carbon matrix. In contrast, TEM images of high MW systems ZnO-$C_{8k\text{-}2}$ and ZnO-$C_{8k\text{-}2.5}$ (see Fig. 2d and f) displayed a distinctively larger particle size of 25–35 nm. These results agree with the values obtained from calculation based on XRD patterns (see Fig. 1) and thus confirm the more pronounced particle aggregation in the high MW matrix. Particle aggregation also induces a distinctive change in the morphology of the ZnO/carbon composite. At similar carbon contents, the ZnO-$C_{8k\text{-}2}$ and ZnO-$C_{8k\text{-}2.5}$ samples exhibited a more porous microstructure (see Fig. 2d and f).

To rationalize the effect of molecular weight on morphology we note that the lower MW PSAN polymer, $M_n - 1{,}800$, has a lower

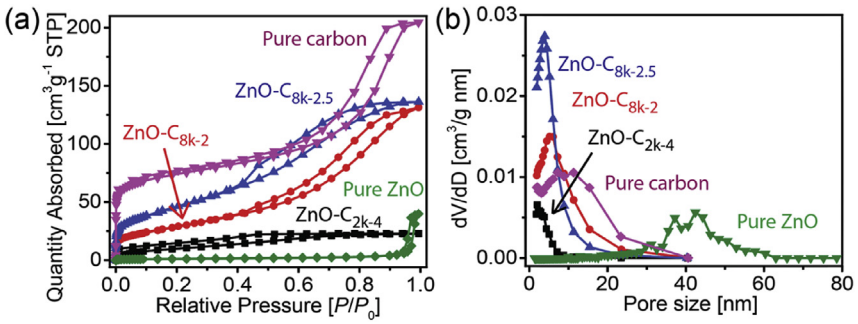

Fig. 3. (a) Comparison of N_2 absorption–desorption isothermal of ZnO-C_{2k-4}, ZnO-C_{8k-2}, ZnO-$C_{8k-2.5}$, pure ZnO and pure carbon, (b) pore size distribution of ZnO-C_{2k-4}, ZnO-C_{8k-2}, ZnO-$C_{8k-2.5}$, pure ZnO and pure carbon.

glass transition temperature ($T_{g,1800}$—58 °C, $T_{g,8000}$—92 °C, see Fig. S6), and thus exhibits greater mobility at a given temperature (this effect is further enhanced by the molecular weight dependence of the diffusion coefficient) [66]. Furthermore, the entropy gain associated with particle dispersion is expected to increase within a lower molecular weight matrix. We therefore hypothesize that in the heating process, the better dispersion of OA-ZnO in low molecular PSAN was more effective in preventing the aggregation or recrystallization of ZnO.

Brunauer-Emmett-Teller (BET) and Barrett-Joyner-Halenda (BJH) methods were also applied to compare specific surface area and pore volume of ZnO/carbon nanocomposites. A type IV isotherm with hysteresis loops at $P/P_0 > 0.4$ was obtained for ZnO-C_{8k-2} and ZnO-$C_{8k-2.5}$, as shown in Fig. 3a. This indicates the existence of large number of mesopores inside the matrix of the ZnO/carbon nanocomposites [67]. The specific surface areas (SSA) of ZnO-C_{2k-4}, ZnO-C_{8k-2}, ZnO-$C_{8k-2.5}$, pure ZnO and pure carbon were 40 $m^2 g^{-1}$, 105 $m^2 g^{-1}$, 170 $m^2 g^{-1}$, 5 $m^2 g^{-1}$, and 244 $m^2 g^{-1}$, respectively. Expectedly, pure carbon exhibited the highest high specific surface area. However, it is important to note that final composition of ZnO/carbon hybrids contain about 90 wt% ZnO. Since ZnO particles barely contributes to specific surface area, if we only consider the specific surface areas from porous carbon structure, remarkably high values of 482 $m^2 g^{-1}$, 1382 $m^2 g^{-1}$, and 2024 $m^2 g^{-1}$ can be estimated for ZnO-C_{8k-4}, ZnO-C_{8k-2} and ZnO-$C_{8k-2.5}$, respectively.

These differences corroborate the expectations based on the distinct microstructure within the ZnO/carbon nanocomposites. In addition, BJH pore size distribution illustrated the presence of a large number of mesopores (with diameter from 2 nm to 50 nm) and nanopores (with diameter less than 2 nm) in the carbon formed from ZnO-$C_{8k-2.5}$. These mesopores could act as electrolyte reservoirs during the electrochemical tests which should lead to better capacitive performance. For both pure ZnO and pure carbon samples, the specific volumes of nanopores were distinctly lower than ZnO/carbon composites. For ZnO, we attribute this result to densification as a consequence of particle aggregation. For pure carbon, we hypothesize that the absence of ZnO particles as hard temples hindered the formation of nanoporous carbon structure (see Table 2).

Highly porous, conductive structures are particularly suitable for the preparation of pseudocapacitor electrodes. The electrochemical performance of ZnO/carbon nanocomposites was determined using a two-electrode system and the results are shown in Fig. 4. The results were also compared with reference electrodes consisting of ZnO and porous carbon respectively. In Fig. 4a, the CV curves were compared at scan rate of 100 mV s^{-1}. Compared with ZnO-C_{2k-4} and ZnO-C_{8k-2}, the ZnO-$C_{8k-2.5}$ system shows symmetric rectangular CV curves. This was attributed to lower internal resistance of ZnO-$C_{8k-2.5}$. The comparison of the specific capacitances measured at different scan rate reveals that higher specific capacitance and better rate performance were obtained with ZnO-$C_{8k-2.5}$ (Fig. 4b). At 2 mV s^{-1}, mean specific capacitance of electrodes from samples ZnO-C_{2k-4}, ZnO-C_{8k-2}, and ZnO-$C_{8k-2.5}$ reached 49 F g^{-1}, 123 F g^{-1}, and 145 F g^{-1}, respectively. Presumably the main reason of this difference in performance is the presence of a more developed contact area between ZnO and electrolyte and a larger specific surface area of electrodes prepared from ZnO-$C_{8k-2.5}$. In addition, the presence of mesopores inside the ZnO/carbon structure leads to better ionic diffusion by acting as reservoirs for the electrolyte [6]. As expected, pure ZnO showed low capacitance (30 F g^{-1} at 2 mV s^{-1}) which is due to high internal resistance and aggregation of ZnO particles without porous carbon structure. It leads to low contact area with electrolyte and long diffusion lengths for ions. Also, the pure carbon from PSAN exhibited low specific capacitance as 21 F g^{-1} at 2 mV s^{-1} despite of its relatively high specific area compared with other samples (as shown in Fig. 3). This too is an expected result that is attributed to the lack of pseudocapacitance from ZnO. Also without ZnO nanoparticles as template, pure carbon samples are expected to suffer from shortage of nanopores to support binding of ions.

Galvanostatic charge–discharge (GCD) tests were applied to evaluate the performance and cycle-life of materials. The GCD performances of ZnO-C_{2k-4}, ZnO-C_{8k-2} and ZnO-$C_{8k-2.5}$ were compared with current density of 0.2 A g^{-1} (see Fig. 4c). The electrode based on ZnO-C_{2k-4} displayed a larger IR drop than ZnO-C_{8k-2}

Table 2
Summary of ZnO/carbon composites characterization.

Entry	ZnO contents (wt%)[a]	Carbon contents (wt%)[a]	Surface area ($m^2 g^{-1}$)[b]
ZnO-C_{2k-4}	91.7	8.3	40
ZnO-C_{8k-2}	92.4	7.6	105
ZnO-$C_{8k-2.5}$	91.6	8.4	170
Pure ZnO	100	0	5
Pure carbon	0	100	244

[a] Inorganic content was determined by TGA.
[b] Surface area was characterized by BET.

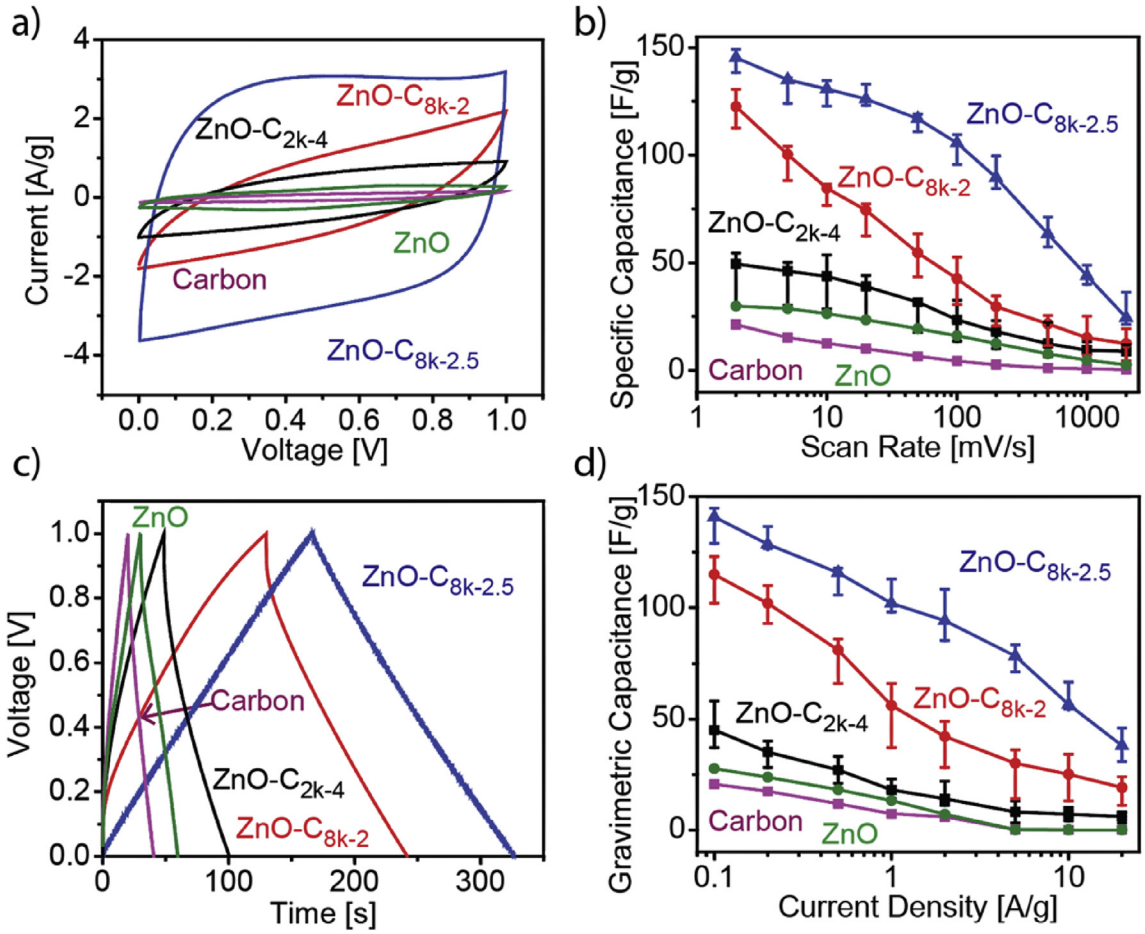

Fig. 4. (a) CV curves of samples ZnO-C_{2k-4}, ZnO-C_{8k-2}, ZnO-$C_{8k-2.5}$, pure ZnO nanoparticles and pure carbon from PSAN at 100 mV s^{-1} compared with electrodes with ZnO and porous carbon; (b) Comparison of specific capacitance from CV curves from 2 mV s^{-1} to 2000 mV s^{-1}; (c) GCD curves of samples ZnO-C_{2k-4}, ZnO-C_{8k-2}, ZnO-$C_{8k-2.5}$, pure ZnO nanoparticles and pure carbon from PSAN at current density of 0.2 A g^{-1}; (d) Comparison of specific capacitance from GCD curves from 0.1 A g^{-1} to 20 A g^{-1}.

and ZnO-$C_{8k-2.5}$ which demonstrated the larger internal resistance of the electrodes. This is interpreted as a consequence of the increased fraction of amorphous component and non-porous structure of the carbon that essentially blocked the ionic and electrical transportation. The GCD behavior of ZnO-$C_{8k-2.5}$-based electrode showed symmetric curves from 0.1 A g^{-1} to 20 A g^{-1}, illustrating ideal capacitive properties. The reason of higher capacitance of ZnO-$C_{8k-2.5}$ is attributable to the porous morphology, which provided more active sites for ion adsorption–desorption and faster ionic diffusion. The capacitance relationships of different electrodes were similar in GCD tests (Fig. 4d) as well as in CV tests. The mean specific capacitance ZnO-$C_{8k-2.5}$ reached 141 F g^{-1}, 102 F g^{-1}, and 38 F g^{-1} at current density of 0.1 A g^{-1}, 1 A g^{-1} and 20 A g^{-1}, respectively. Low capacitance of electrodes with pure ZnO

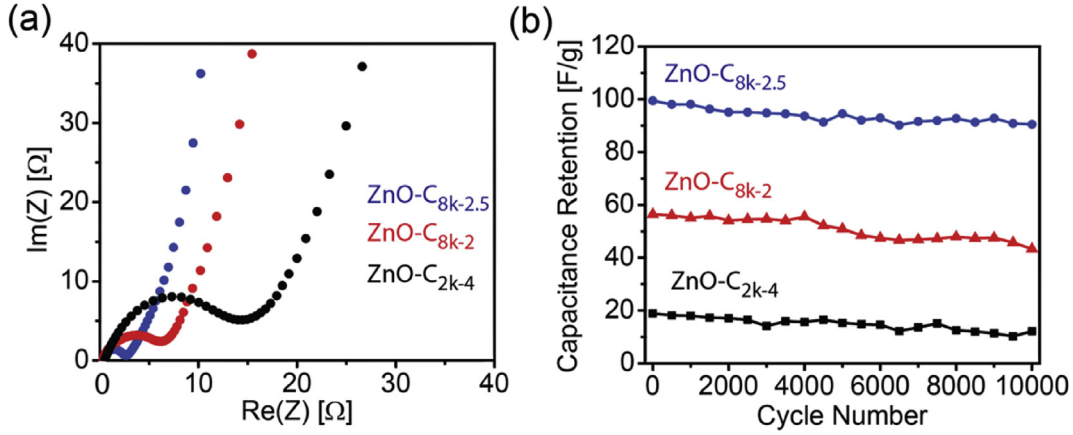

Fig. 5. (a) electrochemical impedance spectra (EIS) of samples ZnO-C_{2k-4}, ZnO-C_{8k-2}, ZnO-$C_{8k-2.5}$; (b) Lifetime tests of samples ZnO-C_{2k-4}, ZnO-C_{8k-2}, ZnO-$C_{8k-2.5}$ with current density of 1 A g^{-1}.

and pure carbon again confirmed the synergistic effect of ZnO/carbon hybrid materials.

Next, electrochemical impedance spectroscopy (EIS) was used to evaluate the electrical and ionic transport characteristics of the ZnO/carbon hybrids as Nyquist plots in Fig. 5a. The shape of Nyquist plots is consistent with two-electrode configuration. In the high frequency region, the curves showed negligible cells characteristic electrolyte resistance (R_S), lower than 0.2 Ω. The semicircles in the middle frequency region demonstrated differences in the internal resistances of electrodes prepared from ZnO-C_{2k-4} (15.9 Ω), ZnO-C_{8k-2} (6.4 Ω), to ZnO-$C_{8k-2.5}$ (2.0 Ω) [68]. This difference should be attributed to the mesoporous structure of the ZnO-$C_{8k-2.5}$ based carbon which led to higher conductivity and better ionic diffusion in the electrolyte. At low-frequency region, the approximately vertical trend of the data illustrated ideal ion diffusion of the ZnO-$C_{8k-2.5}$ electrodes in electrolyte.

Finally, lifetime tests were applied with current density of 1 A g^{-1} to access the durability of ZnO/carbon nanocomposites. Electrodes based on ZnO-C_{2k-4}, ZnO-C_{8k-2} and ZnO-$C_{8k-2.5}$ maintained 64%, 77%, and 91% of their initial capacitance after 10,000 charge-discharge cycles, respectively (Fig. 5b). Compared with other ZnO based pseudocapacitors reported in the literature (see Table S1), the retention of 91% after 10,000 cycles is remarkable. This high stability is attributed to the synergistic realization of mechanical stability of nanoporous carbon structures derived by PSAN copolymers as well as highly porous tunnels for ionic diffusion.

4. Conclusions

In summary, random co-polymerization of acrylonitrile (AN) and styrene (S) enables the solution processing of ZnO/PSAN composite films that can be pyrolyzed to form ZnO/carbon hybrid materials. Structure formation during pyrolysis is found to be sensitive to the molecular weight to matrix polymers. More uniform microstructures are observed for lower MW matrix polymers while higher MW PSAN promotes the coarsening of ZnO crystallites and the formation of more porous hybrid morphologies. Molecular weight thus provides a gauge to control the microstructure (and thus electrochemical performance) of ZnO/carbon hybrids. More porous structures were found to exhibit better performance in pseudocapacitor applications. ZnO/carbon composite electrodes derived from high MW PSAN exhibited a maximum specific capacitance as high as 145 F g^{-1}, at the scan rate of 2 mV s^{-1} in the presence of a KOH electrolyte. Furthermore, the specific capacitance was maintained at 91% of its initial values after 10,000 successive charge/discharge cycles, which demonstrated its outstanding cycling stability. The simple synthesis method, competitive electrochemical capacitance, and high stability indicated its promising prospect as a pseudocapacitor electrode. Finally, given the wide range of materials that are amenable to SI-ATRP, we expect the presented approach to be applicable to enable the synthesis of a wide range of transition metal oxide/carbon hybrids [69,70].

Conflicts of interest

The authors declare no competing financial interest.

Acknowledgements

This work was supported by NSF (Grants DMR 1501324 and CMMI 1663305), as well as the Scott Institute for Energy Technologies at Carnegie Mellon University.

Appendix A. Supplementary data

Supplementary data related to this article can be found at https://doi.org/10.1016/j.polymer.2018.01.024.

References

[1] P. Simon, Y. Gogotsi, Materials for electrochemical capacitors, Nat. Mater. 7 (11) (2008) 845–854.
[2] C. Liu, F. Li, L.P. Ma, H.M. Cheng, Advanced materials for energy storage, Adv. Mater. 22 (8) (2010) E28–E62.
[3] G. Wang, L. Zhang, J. Zhang, A review of electrode materials for electrochemical supercapacitors, Chem. Soc. Rev. 41 (2) (2012) 797–828.
[4] L.L. Zhang, X. Zhao, Carbon-based materials as supercapacitor electrodes, Chem. Soc. Rev. 38 (9) (2009) 2520–2531.
[5] Z. Yang, J. Zhang, M.C.W. Kintner-Meyer, X. Lu, D. Choi, J.P. Lemmon, J. Liu, Electrochemical energy storage for Green grid, Chem. Rev. 111 (5) (2011) 3577–3613.
[6] M.D. Stoller, S. Park, Y. Zhu, J. An, R.S. Ruoff, Graphene-based ultracapacitors, Nano Lett. 8 (10) (2008) 3498–3502.
[7] Z.-S. Wu, W. Ren, D.-W. Wang, F. Li, B. Liu, H.-M. Cheng, High-energy MnO2 nanowire/graphene and graphene asymmetric electrochemical capacitors, ACS Nano 4 (10) (2010) 5835–5842.
[8] J. Jiang, Y. Li, J. Liu, X. Huang, C. Yuan, X.W. Lou, Recent advances in metal oxide-based electrode architecture design for electrochemical energy storage, Adv. Mater. 24 (38) (2012) 5166–5180.
[9] Y. Zhao, M.P. Li, S. Liu, M.F. Islam, Superelastic pseudocapacitors from free-standing MnO2 decorated graphene-coated carbon nanotube aerogels, ACS Appl. Mater. Interfaces 9 (28) (2017) 23810–23819.
[10] Y. Zhang, H. Feng, X. Wu, L. Wang, A. Zhang, T. Xia, H. Dong, X. Li, L. Zhang, Progress of electrochemical capacitor electrode materials: a review, Int. J. Hydrogen Energy 34 (11) (2009) 4889–4899.
[11] M. Vangari, T. Pryor, L. Jiang, Supercapacitors: review of materials and fabrication methods, J. Energy Eng. 139 (2) (2012) 72–79.
[12] V. Augustyn, P. Simon, B. Dunn, Pseudocapacitive oxide materials for high-rate electrochemical energy storage, Energy Environ. Sci. 7 (5) (2014) 1597–1614.
[13] D.-W. Wang, F. Li, H.-M. Cheng, Hierarchical porous nickel oxide and carbon as electrode materials for asymmetric supercapacitor, J. Power Sources 185 (2) (2008) 1563–1568.
[14] M. Mastragostino, C. Arbizzani, F. Soavi, Polymer-based supercapacitors, J. Power Sources 97–98 (2001) 812–815.
[15] S. Grover, S. Goel, V. Sahu, G. Singh, R.K. Sharma, Asymmetric supercapacitive characteristics of pani embedded holey graphene nanoribbons, ACS Sustain. Chem. Eng. 3 (7) (2015) 1460–1469.
[16] W. Chen, R. Rakhi, H.N. Alshareef, Facile synthesis of polyaniline nanotubes using reactive oxide templates for high energy density pseudocapacitors, J. Mater. Chem. 1 (10) (2013) 3315–3324.
[17] T. Liu, L. Finn, M. Yu, H. Wang, T. Zhai, X. Lu, Y. Tong, Y. Li, Polyaniline and polypyrrole pseudocapacitor electrodes with excellent cycling stability, Nano Lett. 14 (5) (2014) 2522–2527.
[18] X. Cai, S.H. Lim, C.K. Poh, L. Lai, J. Lin, Z. Shen, High-performance asymmetric pseudocapacitor cell based on cobalt hydroxide/graphene and polypyrrole/graphene electrodes, J. Power Sources 275 (2015) 298–304.
[19] Y. Hou, L. Chen, L. Zhang, J. Kang, T. Fujita, J. Jiang, M. Chen, Ultrahigh capacitance of nanoporous metal enhanced conductive polymer pseudocapacitors, J. Power Sources 225 (2013) 304–310.
[20] J. Han, M. Wang, Y. Hu, C. Zhou, R. Guo, Conducting polymer-noble metal nanoparticle hybrids: synthesis mechanism application, Prog. Polym. Sci. 70 (2017) 52–91.
[21] L. Hu, J.W. Choi, Y. Yang, S. Jeong, F. La Mantia, L.-F. Cui, Y. Cui, Highly conductive paper for energy-storage devices, Proc. Natl. Acad. Sci. Unit. States Am. 106 (51) (2009) 21490–21494.
[22] D. Wang, Y. Li, Q. Wang, T. Wang, Nanostructured Fe2O3–graphene composite as a novel electrode material for supercapacitors, J. Solid State Electrochem. 16 (6) (2012) 2095–2102.
[23] J. Liu, M. Lu, J. Yang, J. Cheng, W. Cai, Capacitive desalination of ZnO/activated carbon asymmetric capacitor and mechanism analysis, Electrochim. Acta 151 (2015) 312–318.
[24] D. Lan, Y. Chen, P. Chen, X. Chen, X. Wu, X. Pu, Y. Zeng, Z. Zhu, Mesoporous CoO nanocubes@ continuous 3D porous carbon skeleton of rose-based electrode for high-performance supercapacitor, ACS Appl. Mater. Interfaces 6 (15) (2014) 11839–11845.
[25] X.-H. Xia, J.-P. Tu, X.-L. Wang, C.-D. Gu, X.-B. Zhao, Mesoporous Co3O4 monolayer hollow-sphere array as electrochemical pseudocapacitor material, Chem. Commun. 47 (20) (2011) 5786–5788.
[26] L. Hu, W. Chen, X. Xie, N. Liu, Y. Yang, H. Wu, Y. Yao, M. Pasta, H.N. Alshareef, Y. Cui, Symmetrical MnO2–carbon nanotube–textile nanostructures for wearable pseudocapacitors with high mass loading, Acs Nano 5 (11) (2011) 8904–8913.
[27] Y. He, W. Chen, X. Li, Z. Zhang, J. Fu, C. Zhao, E. Xie, Freestanding three-dimensional graphene/MnO2 composite networks as ultralight and flexible supercapacitor electrodes, ACS nano 7 (1) (2012) 174–182.
[28] V.D. Punetha, S. Rana, H.J. Yoo, A. Chaurasia, J.T. McLeskey Jr., M.S. Ramasamy,

N.G. Sahoo, J.W. Cho, Functionalization of carbon nanomaterials for advanced polymer nanocomposites: a comparison study between CNT and graphene, Prog. Polym. Sci. 67 (2017) 1–47.
[29] J. Mu, C. Shao, Z. Guo, Z. Zhang, M. Zhang, P. Zhang, B. Chen, Y. Liu, High photocatalytic activity of ZnO–Carbon nanofiber heteroarchitectures, ACS Appl. Mater. Interfac. 3 (2) (2011) 590–596.
[30] Z. Pu, Q. Liu, A.H. Qusti, A.M. Asiri, A.O. Al-Youbi, X. Sun, Fabrication of Ni (OH) 2 coated ZnO array for high-rate pseudocapacitive energy storage, Electrochim. Acta 109 (2013) 252–255.
[31] Z. Xing, Q. Chu, X. Ren, C. Ge, A.H. Qusti, A.M. Asiri, A.O. Al-Youbi, X. Sun, Ni 3 S 2 coated ZnO array for high-performance supercapacitors, J. Power Sources 245 (2014) 463–467.
[32] D. Kalpana, K. Omkumar, S.S. Kumar, N. Renganathan, A novel high power symmetric ZnO/carbon aerogel composite electrode for electrochemical supercapacitor, Electrochim. Acta 52 (3) (2006) 1309–1315.
[33] M. Jayalakshmi, M. Palaniappa, K. Balasubramanian, Single step solution combustion synthesis of ZnO/carbon composite and its electrochemical characterization for supercapacitor application, Int. J. Electrochem. Sci 3 (2008) 96–103.
[34] Y. Zhang, H. Li, L. Pan, T. Lu, Z. Sun, Capacitive behavior of graphene–ZnO composite film for supercapacitors, J. Electroanal. Chem. 634 (1) (2009) 68–71.
[35] Y. Zhang, X. Sun, L. Pan, H. Li, Z. Sun, C. Sun, B.K. Tay, Carbon nanotube–zinc oxide electrode and gel polymer electrolyte for electrochemical supercapacitors, J. Alloy. Comp. 480 (2) (2009) L17–L19.
[36] T. Lu, Y. Zhang, H. Li, L. Pan, Y. Li, Z. Sun, Electrochemical behaviors of graphene–ZnO and graphene–SnO 2 composite films for supercapacitors, Electrochim. Acta 55 (13) (2010) 4170–4173.
[37] T. Lu, L. Pan, H. Li, G. Zhu, T. Lv, X. Liu, Z. Sun, T. Chen, D.H. Chua, Microwave-assisted synthesis of graphene–ZnO nanocomposite for electrochemical supercapacitors, J. Alloy. Comp. 509 (18) (2011) 5488–5492.
[38] J. Wang, Z. Gao, Z. Li, B. Wang, Y. Yan, Q. Liu, T. Mann, M. Zhang, Z. Jiang, Green synthesis of graphene nanosheets/ZnO composites and electrochemical properties, J. Solid State Chem. 184 (6) (2011) 1421–1427.
[39] Y.-L. Chen, Z.-A. Hu, Y.-Q. Chang, H.-W. Wang, Z.-Y. Zhang, Y.-Y. Yang, H.-Y. Wu, Zinc oxide/reduced graphene oxide composites and electrochemical capacitance enhanced by homogeneous incorporation of reduced graphene oxide sheets in zinc oxide matrix, J. Phys. Chem. C 115 (5) (2011) 2563–2571.
[40] C.-T. Hsieh, J.-S. Lin, Y.-F. Chen, C.-Y. Lin, W.-Y. Li, Graphene sheets anchored with ZnO nanocrystals as electrode materials for electrochemical capacitors, Mater. Chem. Phys. 143 (2) (2014) 853–859.
[41] E.R. Ezeigwe, M.T. Tan, P.S. Khiew, C.W. Siong, One-step green synthesis of graphene/ZnO nanocomposites for electrochemical capacitors, Ceram. Int. 41 (1) (2015) 715–724.
[42] X. Xiao, B. Han, G. Chen, L. Wang, Y. Wang, Preparation and electrochemical performances of carbon sphere@ ZnO core-shell nanocomposites for supercapacitor applications, Sci. Rep. 7 (2017).
[43] Y. Zhang, X. Sun, L. Pan, H. Li, Z. Sun, C. Sun, B.K. Tay, Carbon nanotube–ZnO nanocomposite electrodes for supercapacitors, Solid State Ionics 180 (32) (2009) 1525–1528.
[44] N.I.T. Ramli, S.A. Rashid, M.S. Mamat, Y. Sulaiman, S.A. Zobir, S. Krishnan, Incorporation of Zinc Oxide into Carbon nanotube/Graphite nanofiber as high performance supercapacitor electrode, Electrochim. Acta 228 (Supplement C) (2017) 259–267.
[45] M. Epifani, J. Arbiol, R. Díaz, M.J. Perálvarez, P. Siciliano, J.R. Morante, Synthesis of SnO2 and ZnO colloidal nanocrystals from the decomposition of tin(II) 2-ethylhexanoate and zinc(II) 2-ethylhexanoate, Chem. Mater. 17 (25) (2005) 6468–6472.
[46] D. Weber, S. Botnaras, D.V. Pham, J. Steiger, L. De Cola, Functionalized ZnO nanoparticles for thin-film transistors: support of ligand removal by non-thermal methods, J. Mater. Chem. C 1 (18) (2013) 3098–3103.
[47] Z. Wang, Z. Lu, C. Mahoney, J. Yan, R. Ferebee, D. Luo, K. Matyjaszewski, M.R. Bockstaller, Transparent and high refractive index thermoplastic polymer glasses using evaporative ligand exchange of hybrid particle fillers, ACS Appl. Mater. Interfac. 9 (8) (2017) 7515–7522.
[48] Z. Wang, C. Mahoney, J. Yan, Z. Lu, R. Ferebee, D. Luo, M.R. Bockstaller, K. Matyjaszewski, Preparation of well-defined poly(styrene-co-acrylonitrile)/ZnO hybrid nanoparticles by an efficient ligand exchange strategy, Langmuir 32 (49) (2016) 13207–13213.
[49] W. Jakubowski, K. Min, K. Matyjaszewski, Activators regenerated by electron transfer for atom transfer radical polymerization of styrene, Macromolecules 39 (1) (2006) 39–45.
[50] A. Plichta, M. Zhong, W. Li, A.M. Elsen, K. Matyjaszewski, Tuning dispersity in diblock copolymers using ARGET ATRP, Macromol. Chem. Phys. 213 (24) (2012) 2659–2668.
[51] K. Matyjaszewski, Atom transfer radical polymerization (ATRP): current status and future perspectives, Macromolecules 45 (10) (2012) 4015–4039.
[52] P. Chmielarz, M. Fantin, S. Park, A.A. Isse, A. Gennaro, A.J.D. Magenau, A. Sobkowiak, K. Matyjaszewski, Electrochemically mediated atom transfer radical polymerization (eATRP), Prog. Polym. Sci. 69 (Supplement C) (2017) 47–78.
[53] X. Pan, M.A. Tasdelen, J. Laun, T. Junkers, Y. Yagci, K. Matyjaszewski, Photomediated controlled radical polymerization, Prog. Polym. Sci. 62 (Supplement C) (2016) 73–125.
[54] D. Wu, Z. Li, M. Zhong, T. Kowalewski, K. Matyjaszewski, Templated synthesis of nitrogen-enriched nanoporous carbon materials from porogenic organic precursors prepared by ATRP, Angew. Chem. Int. Ed. 53 (15) (2014) 3957–3960.
[55] K. Matyjaszewski, J. Xia, Atom transfer radical polymerization, Chem. Rev. 101 (9) (2001) 2921–2990.
[56] J. Pietrasik, H. Dong, K. Matyjaszewski, Synthesis of high molecular weight poly(styrene-co-acrylonitrile) copolymers with controlled architecture, Macromolecules 39 (19) (2006) 6384–6390.
[57] D. Wu, H. Dong, J. Pietrasik, E.K. Kim, C.M. Hui, M. Zhong, M. Jaroniec, T. Kowalewski, K. Matyjaszewski, Novel nanoporous carbons from well-defined poly(styrene-co-acrylonitrile)-grafted silica nanoparticles, Chem. Mater. 23 (8) (2011) 2024–2026.
[58] M. Kruk, B. Dufour, E.B. Celer, T. Kowalewski, M. Jaroniec, K. Matyjaszewski, Well-defined poly(ethylene oxide)–Polyacrylonitrile diblock copolymers as templates for mesoporous silicas and precursors for mesoporous carbons, Chem. Mater. 18 (6) (2006) 1417–1424.
[59] N.V. Tsarevsky, T. Sarbu, B. Göbelt, K. Matyjaszewski, Synthesis of Styrene–Acrylonitrile copolymers and related block copolymers by atom transfer radical polymerization, Macromolecules 35 (16) (2002) 6142–6148.
[60] B. Sarkar, P. Alexandridis, Block copolymer–nanoparticle composites: structure, functional properties, and processing, Prog. Polym. Sci. 40 (2015) 33–62.
[61] M.D. Stoller, R.S. Ruoff, Best practice methods for determining an electrode material's performance for ultracapacitors, Energy Environ. Sci. 3 (9) (2010) 1294–1301.
[62] E. Frank, L.M. Steudle, D. Ingildeev, J.M. Spörl, M.R. Buchmeiser, Carbon fibers: precursor systems, processing, structure, and properties, Angew. Chem. Int. Ed. 53 (21) (2014) 5262–5298.
[63] M. Zhong, E.K. Kim, J.P. McGann, S.-E. Chun, J.F. Whitacre, M. Jaroniec, K. Matyjaszewski, T. Kowalewski, Electrochemically active nitrogen-enriched nanocarbons with well-defined morphology synthesized by pyrolysis of self-assembled block copolymer, J. Am. Chem. Soc. 134 (36) (2012) 14846–14857.
[64] D.V. Lam, K. Jo, C.-H. Kim, J.-H. Kim, H.-J. Lee, S.-M. Lee, Activated carbon textile via chemistry of metal extraction for supercapacitors, ACS Nano 10 (12) (2016) 11351–11359.
[65] H.J.T. Ellingham, Reducibility of oxides and sulphides in metallurgical processes, J. Soc. Chem. Ind. (J. Chem. Technol. Biotechnol.) 10 (1944) 125–133.
[66] G.R. Strobl, The Physics of Polymers: Concepts for Understanding their Structures and Behavior, Springer, Berlin Heidelberg, 2013.
[67] S. Gregg, Mesoporous solids: the Type IV isotherm, Adsorpt. Surf. Area Porosity (1982) 137–143.
[68] P. Taberna, P. Simon, J.-F. Fauvarque, Electrochemical characteristics and impedance spectroscopy studies of carbon-carbon supercapacitors, J. Electrochem. Soc. 150 (3) (2003) A292–A300.
[69] C.M. Hui, J. Pietrasik, M. Schmitt, C. Mahoney, J. Choi, M.R. Bockstaller, K. Matyjaszewski, Surface-initiated polymerization as an enabling tool for multifunctional (Nano-)Engineered hybrid materials, Chem. Mater. 26 (1) (2014) 745–762.
[70] J. Yan, X. Pan, Z. Wang, Z. Lu, Y. Wang, L. Liu, J. Zhang, C. Ho, M.R. Bockstaller, K. Matyjaszewski, A fatty acid-inspired tetherable initiator for surface-initiated atom transfer radical polymerization, Chem. Mater. 29 (11) (2017) 4963–4969.